Particles I

Access the latest eBook →

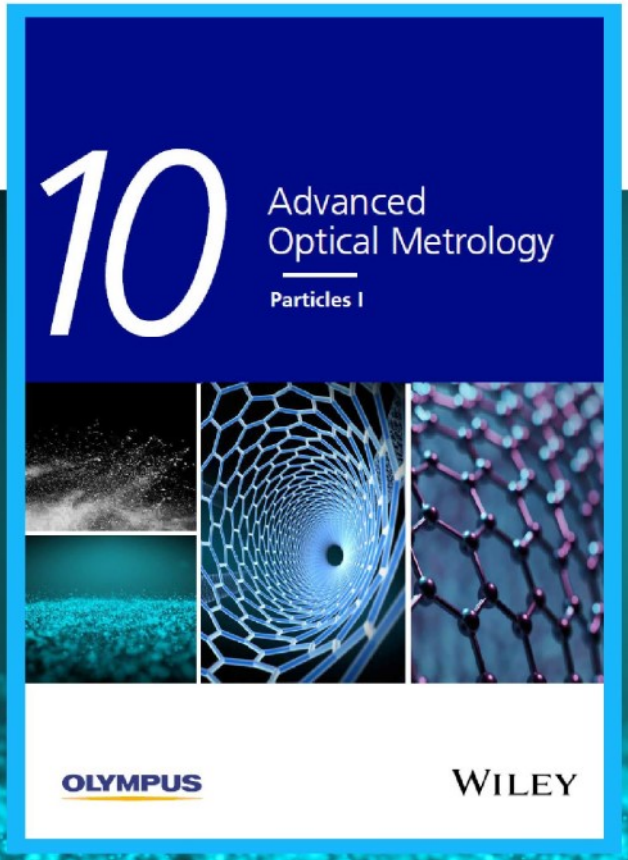

Particles: Unique Properties, Uncountable Applications

Read the latest eBook and better your knowledge with highlights from the recent studies on the design and characterization of micro- and nanoparticles for different application areas.

Access Now

This eBook is sponsored by

OLYMPUS

WILEY

ADVANCED MATERIALS
www.advmat.de

Two-Pronged Intracellular Co-Delivery of Antigen and Adjuvant for Synergistic Cancer Immunotherapy

Junli Meng, Peisen Zhang, Qizhe Chen, Zihua Wang, Yuan Gu, Jie Ma, Wang Li, Chen Yang, Yuanyuan Qiao, Yi Hou, Lihong Jing, Yong Wang, Zi Gu, Lichong Zhu, Haozhen Xu, Xueguang Lu, and Mingyuan Gao**

Nanovaccines have emerged as promising alternatives or complements to conventional cancer treatments. Despite the progresses, specific co-delivery of antigen and adjuvant to their corresponding intracellular destinations for maximizing the activation of antitumor immune responses remains a challenge. Herein, a lipid-coated iron oxide nanoparticle is delivered as nanovaccine (IONP-C/O@LP) that can co-deliver peptide antigen and adjuvant (CpG DNA) into cytosol and lysosomes of dendritic cells (DCs) through both membrane fusion and endosome-mediated endocytosis. Such two-pronged cellular uptake pattern enables IONP-C/O@LP to synergistically activate immature DCs. Iron oxide nanoparticle also exhibits adjuvant effects by generating intracellular reactive oxygen species, which further promotes DC maturation. IONP-C/O@LP accumulated in the DCs of draining lymph nodes effectively increases the antigen-specific T cells in both tumor and spleen, inhibits tumor growth, and improves animal survival. Moreover, it is demonstrated that this nanovaccine is a general platform of delivering clinically relevant peptide antigens derived from human papilloma virus 16 to trigger antigen-specific immune responses in vivo.

1. Introduction

Cancer immunotherapies that combat cancer by manipulating the patients' own immune systems have become promising alternatives or complements to conventional cancer treatments in clinic.[1] Among the immunotherapies, vaccines that harness dendritic cells (DCs) to activate naïve T cells and induce the cytotoxic T lymphocyte (CTL) immune responses have attracted increasing attentions.[2] In principle, DCs can be activated by administrating free antigens and adjuvants.[1a] However, the rapid clearance and enzymatic degradation of antigens and adjuvants limit their efficacy and may lead to off-target toxicity.[3] Additionally, antigens and adjuvants usually take different pathways to stimulate DCs due to their different activation patterns, thus requiring distinct delivery routes. For example, the major histocompatibility complex (MHC) class I-restricted peptide antigens are mainly presented in the cytosol, thus the antigens need to enter cytosol to elicit immune responses.[4] In contrast, the adjuvant such as short single-stranded oligodeoxynucleotides containing unmethylated cytosine-phosphate-guanine motifs (CpG), known as a Toll-like receptor 9 (TLR9) agonist, interacts with TLR9 on the lysosomal membrane to activate myeloid differentiation primary-response protein 88 (MyD88) and downstream nuclear factor kappa-B pathways.[5] Therefore, the lysosomal pathway is preferable for the delivery of CpG.

Nanovaccines have shown potentials for improving the stability and enabling the co-delivery of antigen and adjuvant.[6] For example, liposome encapsulated with antigen and adjuvant is one of the most classic nanovaccines and has entered clinical trials (Stimuvax).[7] Inorganic nanoparticles, such as iron oxide nanoparticles, have also been developed as carriers for delivering antigen and adjuvant.[8] Despite the progresses, most of the reported nanovaccines enter cells through

J. Meng, P. Zhang, Q. Chen, Z. Wang, W. Li, C. Yang, Y. Qiao, Y. Hou, L. Jing, L. Zhu, X. Lu, M. Gao
Key Laboratory of Colloid
Interface and Chemical Thermodynamics
Institute of Chemistry
Chinese Academy of Sciences
Beijing 100190, China
E-mail: xueguang@iccas.ac.cn; gaomy@iccas.ac.cn

J. Meng, P. Zhang, W. Li, C. Yang
School of Chemistry and Chemical Engineering
University of Chinese Academy of Sciences
Beijing 100049, China

The ORCID identification number(s) for the author(s) of this article can be found under https://doi.org/10.1002/adma.202202168.

Y. Gu, J. Ma, Y. Wang, M. Gao
Center for Molecular Imaging and Nuclear Medicine School for Radiological and Interdisciplinary Sciences (RAD-X)
Soochow University
Suzhou 215123, China

Z. Gu
School of Chemical Engineering and Australian Centre for NanoMedicine (ACN)
University of New South Wales
Sydney, NSW 2052, Australia

H. Xu
School of Mathematical and Statistical Sciences
Arizona State University
Tempe, AZ 85287-1804, USA

DOI: 10.1002/adma.202202168

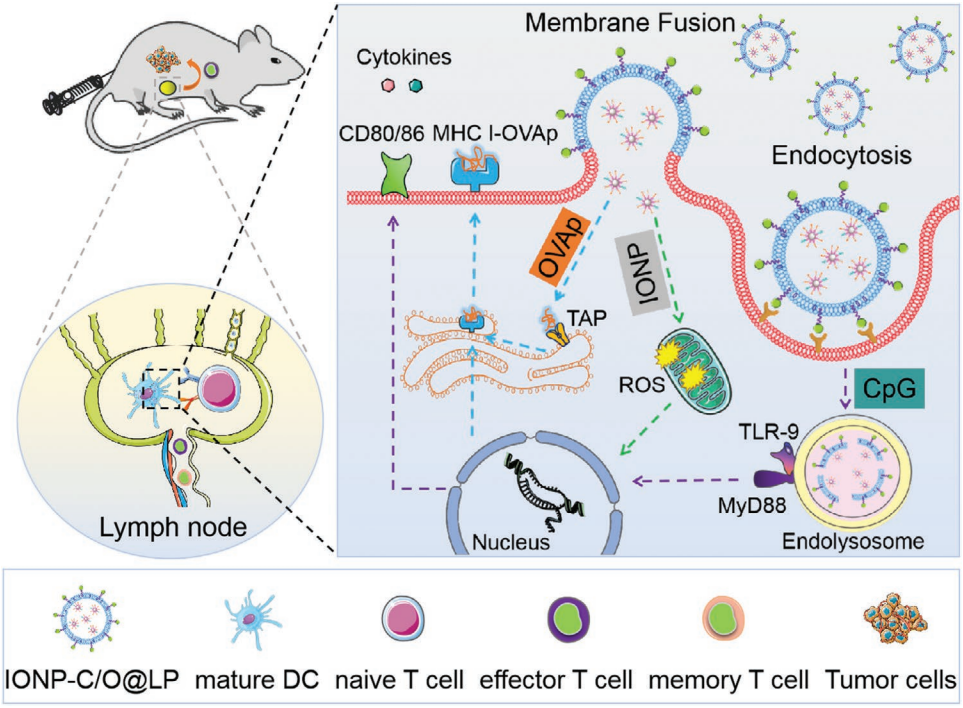

Scheme 1. Schematic illustration showing the synergistic effects and immune responses elicited by IONP-C/O@LP. Specifically, the IONP-C/O@LP deliver OVAp and CpG into iDCs through membrane fusion and endosome-mediated endocytosis, respectively, to synergistically improve the efficacy of DC activation, while Fe_3O_4 nanoparticles further promote the activation of DCs by producing ROS. After subcutaneous injection, IONP-C/O@LP accumulated in the draining lymph node will efficiently enter and subsequently activate iDCs to elicit both local and systemic antitumor immune responses.

endosome-mediated endocytosis.[9] Instability in endosomal environment and poor endosomal escape efficiency of nanoparticles lead to low efficacy of intracellular processing and downstream extracellular presentation of antigens.[10] Nanoparticles that directly enter cytosol through membrane fusion are ideal for delivering antigens, but are not preferred for delivering certain adjuvant, such as CpG, as mentioned above.[11] Therefore, a simple nanoparticle formulation that can simultaneously deliver the antigen and adjuvant into the cytosol and lysosomes of DCs, respectively, is very much needed to maximize the efficacy of antigen and adjuvant.

Herein, we present a nanovaccine that is expected to simultaneously deliver antigen and adjuvant to different intracellular compartments for augmented immune responses as schematically shown in **Scheme 1**. In this nanovaccine, CpG and ovalbumin$_{257\text{-}264}$ peptide (OVAp) were conjugated to magnetic iron oxide nanoparticles (IONP) to yield IONP-C/O conjugates, which were subsequently encapsulated by lipid film (abbreviated as L) bearing a DC-targeting cyclic peptide P30 (abbreviated as P) to form a pomegranate-like nanovaccine, denoted as IONP-C/O@LP. We found that P30 modification changed the cellular uptake pathway of liposomes from solely endosome-mediated endocytosis to a two-pronged uptake pathway involving both endosome-mediated endocytosis and membrane fusion. In consequence, OVAp and CpG were delivered into cytosol and lysosome of immature DCs (iDCs), respectively, which synergistically improved the efficacy of DC activation. IONP not only endowed the nanovaccine with detectability via magnetic resonance imaging (MRI), but also exhibited adjuvant effects by generating intracellular reactive oxygen species (ROS). After subcutaneous injection, IONP-C/O@LP accumulated in the draining lymph node could efficiently enter and activate iDCs, which elicited both local and systemic antitumor immune responses to inhibit tumor growth as either a therapeutic or a prophylactic vaccine. Moreover, the delivery of a clinically relevant peptide antigen derived from human papilloma virus 16 was also demonstrated both in vitro and in vivo to verify the feasibility of the current nanovaccine design for potential clinical application. Therefore, our delivery strategy could enhance the antitumor immune responses of peptide antigens.

2. Results and Discussion

2.1. Preparation and Characterization of IONP-C/O@LP

The preparative procedures of IONP-C/O@LP are schematically shown in **Figure 1**a. In brief, Fe_3O_4 nanoparticles were synthesized via a thermal decomposition method according to our previous work.[12] The average size of the as-prepared IONP is 11.4 ± 1.8 nm according to the transmission electron microscopy (TEM) image given in Figure 1b. Polyethylene glycol (PEG) bearing a diphosphonate group at one end and a maleimide group at the other end (denoted as dip-PEG-mal) was used to replace the oleic acid ligand of Fe_3O_4 particles to obtain water-soluble IONP. Then, thiol-modified CpG (20 equiv.) and OVAp (500 equiv.) were conjugated to maleimide-PEG-IONP (1 equiv.) to yield IONP-C/O (Figure 1c). Dynamic light scattering (DLS) analysis shows that the coupling of CpG and OVAp on the

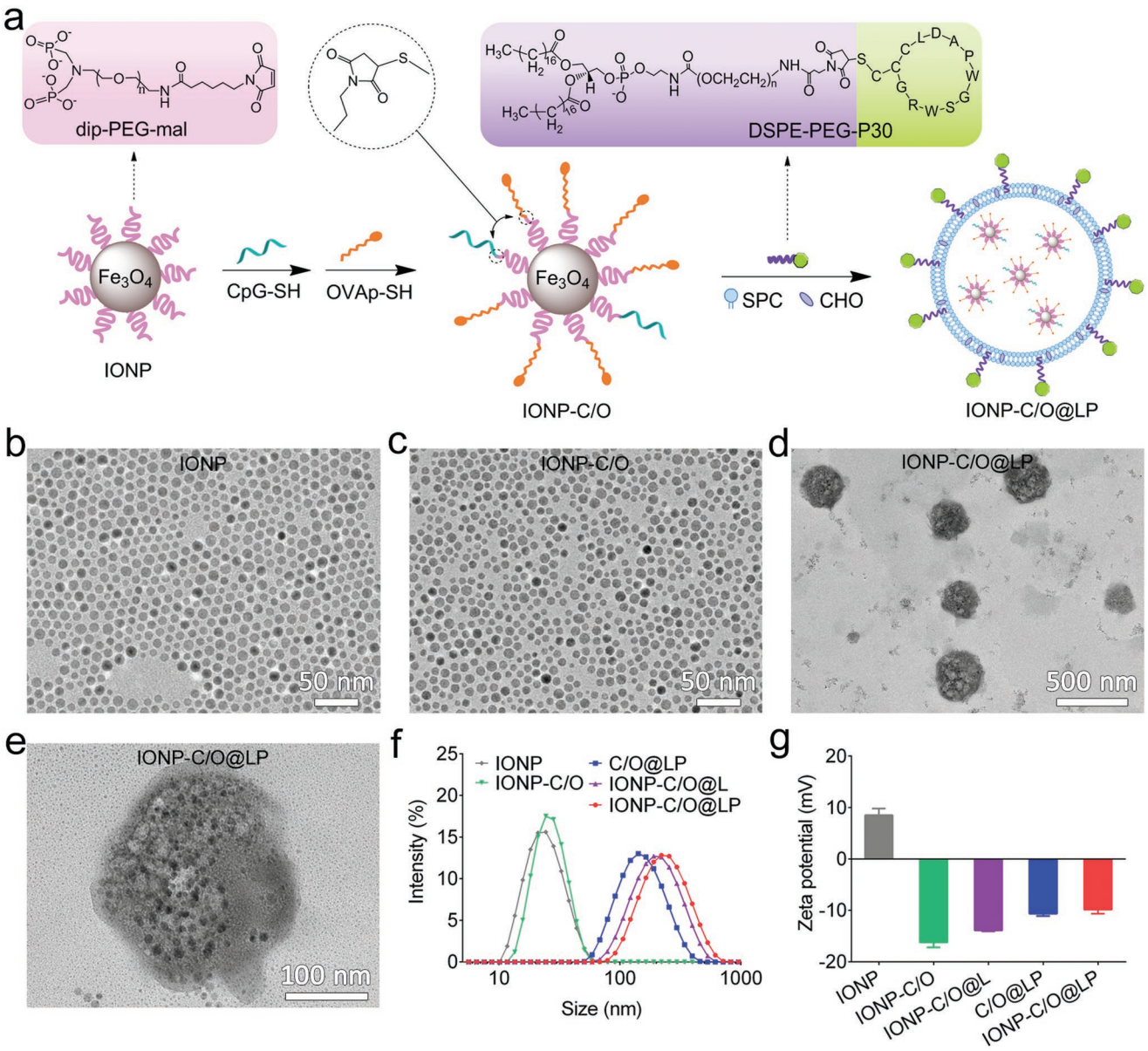

Figure 1. a) Schematic drawing to show the preparative procedures for IONP-C/O@LP. b–e) TEM images of IONP, IONP-C/O conjugates, and IONP-C/O@LP under different magnifications, respectively. f,g) Hydrodynamic size profiles and zeta potentials of IONP, IONP-C/O, IONP-C/O@L, C/O@LP, IONP-C/O@LP nanoformulations, respectively. Data are shown as mean ± SD (n = 3).

surface of PEGylated IONP slightly increase the hydrodynamic size from ≈22.5 to ≈27.9 nm, but barely broaden the particle size distribution, as shown in Figure 1f. The conjugation yields for CpG and OVAp are determined to be ≈78% and 64%, respectively (Figure S1, Supporting Information). Accordingly, the molar ratio of IONP:CpG:OVAp in IONP-C/O was ≈1:16:320.

Thiol-modified P30 peptide that can specifically bind with highly expressed integrin cluster of differentiation (CD) 11c/CD18 on DC membranes was conjugated to 1,2-distearoyl-sn-glycero-3-phosphorylethanolamine-PEG-maleimide (DSPE-PEG-mal) to obtain DSPE-PEG-P30.[13] Successful conjugation was confirmed by matrix-assisted laser desorption/ionization time-of-flight mass spectrometry (MALDI-TOF-MS, Figure S2, Supporting Information). IONP-C/O conjugates were encapsulated in liposomes (soybean phosphatidylcholine:cholesterol:DSPE-PEG-P30 = 10:6:1) to obtain IONP-C/O@LP following a film hydration method.[14] TEM and scanning electron microscopy (SEM) results show that IONP-C/O@LP are uniform spheres loaded with dozens of IONP-C/O distributed throughout the liposomes (Figure 1d,e and Figure S3, Supporting Information), which is consistent with previous publications.[14a,15] With respect to the control particles formed by directly coating the PEGylated IONPs with lipids, they present irregular morphologies as shown in Figure S4 (Supporting Information). This is probably because PEG-rich surface has very low surface energy.[16] Although the complicated interactions between the PEGylated IONPs and the components in the lipid formulation lead to particle aggregation, it is not necessary

for the resulting particle aggregates to form spherical shape to further reduce the surface energy, contrasting to PEGylated particles simultaneously coated with OVAp and CpG. The hydrodynamic diameter dramatically increases from ≈27.9 to ≈197.3 nm after encapsulation (Figure 1f). The encapsulation efficiency of IONP is ≈65% estimated by comparing the iron contents determined before and after encapsulation. The surface potential also varies accordingly from +8.53 mV for PEGylated IONP to −16.42 mV for IONP-C/O, and to −10.15 mV for IONP-C/O@LP (Figure 1g), further confirming the successful hierarchical construction of the IONP-C/O@LP. IONP-C/O@LP present nearly unchanged size and surface potential in 1× phosphate buffered saline (PBS) with 10% fetal bovine serum (FBS) over 6 d (Figure S5, Supporting Information), indicating good colloidal stability under physiological conditions.

2.2. Cellular Uptake Ability and Cytotoxicity of IONP-C/O@LP In Vitro

Prussian blue staining and inductively coupled plasma mass spectrometry (ICP-MS) were used to detect the intracellular Fe level qualitatively and quantitatively after IONP-C/O@LP were incubated with DCs. IONP-C/O@LP group presents the highest DC uptake among all groups at concentration of 50 μg Fe mL^{-1}, as shown in **Figure 2**a,b, and keeps high delivery efficiency at a concentration as low as 10 μg Fe mL^{-1} (Figure S6, Supporting Information). The cellular uptake amount of IONP gradually increased upon lipid encapsulation (IONP-C/O@L) followed by P30 modification (IONP-C/O@LP), suggesting that both lipid encapsulation and P30 peptide contribute to the cellular uptake of IONP-C/O@LP. Flow cytometry was used to detect the fluorescence signal of Cyanine5.5 (Cy5.5)-labeled OVAp in DCs. As shown in Figure 2c, IONP-C/O@LP present the highest cellular uptake, which is consistent with ICP-MS results. Notably, the cellular uptake of IONP-C/O@LP is ≈1.6-fold over that of C/O@LP, indicating that IONP also contributes to cellular uptake of IONP-C/O@LP. To visualize the intracellular localization of IONP-C/O@LP, the lipid films were stained with 1,1′-dioctadecyl-3,3,3′,3′-tetramethyl-indodicarbocyanine perchlorate (DiD). IONP-C/O@LP were incubated with DCs and imaged by confocal laser scanning microscopy. Lysosomes were stained by LysoTracker Green before imaging. The results given in Figure 2d,e reveal that IONP-C/O@LP (red) are widely distributed in different cell compartments including cell membrane and lysosomes, while the nanoformulation involving no targeting peptide (IONP-C/O@L) are found exclusively in lysosomes (green). Quantitative analysis in Figure 2f showed that only approximately 31% of IONP-C/O@LP were found in lysosomes, whereas ≈99% of IONP-C/O@L were observed in lysosomes. To further disclose the intracellular delivery pathway of IONP-C/O@LP and IONP-C/O@L, DCs were treated with membrane fusion inhibitor (methyl-β-cyclodextrin, MBCD), or endocytosis inhibitors including wortmannin (Wort) and chlorpromazine (CPM), or both,[17] before incubating with IONP-C/O@LP or IONP-C/O@L. OVAp was labeled with fluorescein isothiocyanate (FITC) for flow cytometric analysis. As shown in Figure 2g,h and Figure S7 (Supporting Information), MBCD and Wort+CPM treatments significantly decrease the quantity of internalized IONP-C/O@LP from ≈80% for untreated group to ≈43% and 30%, respectively. MBCD+Wort+CPM treatment further decreases the amount of internalized IONP-C/O@LP to approximately 16%, indicating that IONP-C/O@LP enter cells through both membrane fusion and endocytosis. In contrast, MBCD treatment exhibits negligible inhibition for the delivery of IONP-C/O@L compared to untreated group (Figure 2h). Wort+CPM treatment substantially inhibits the uptake of IONP-C/O@L similar to MBCD+Wort+CPM group, indicating that IONP-C/O@L enter cells predominantly through endosome-medicated endocytosis. Collectively, these results demonstrate that P30 peptide changes the cellular uptake pathway of nanovaccine from solely endosome-mediated endocytosis to a two-pronged uptake mechanism: membrane fusion and endosome-mediated endocytosis. Such two-pronged cellular uptake pathway is preferred for maximized immune response activation because OVAp and CpG need to be delivered to cytosol for antigen presentation and endosome for TLR9 activation, respectively.

The cytotoxicity of IONP-C/O@LP to DC was evaluated by methyl thiazolyl tetrazolium (MTT) assay. All tested groups did not show significant cytotoxicity even at high concentration of 200 μg Fe mL^{-1}, as shown in Figure S8 (Supporting Information), ≈50-fold of the dose used in the following in vivo experiments. These results indicate that the IONP-C/O@LP could serve as a safe vehicle for the delivery of antigen and adjuvant.

2.3. Activation of DCs by Nanovaccines In Vitro

After capturing antigens, DCs will mature into immunostimulatory DCs with upregulated expression of costimulatory molecules, enhanced antigen presentation, and increased secretion of proinflammatory cytokines.[2a,18] The expression of costimulatory molecules CD86 (one of the hallmarks of DC maturity) and presentation of MHC I-restricted OVAp (SIINFEKL) on the membrane of DCs after incubation with different groups were analyzed via flow cytometry.[9a,19] As shown in **Figure 3**a,b, IONP-C/O@LP treatment increases the population of $CD86^+$ DCs and H-$2K^b$(SIINFEKL)$^+$ DCs by ≈1.3 and 2.3 times compared to IONP-C/O@L treatment, respectively, indicating the two-pronged cellular uptake pathway improves the efficacy of DC activation and antigen presentation. Furthermore, IONP-C/O@LP and IONP-C/O treatments increase $CD86^+$ DCs by 12% and 10% compared to C/O@LP and free C/O treatments (controls without IONP), respectively. IONP by itself also increases the activated DC population compared to PBS-treated group. These data support the adjuvant effect of IONP on activating DCs. The proinflammatory cytokines [Interleukin (IL)-12p70 and IL-6] were determined by enzyme-linked immunosorbent assay (ELISA). The results given in Figure 3c,d reveal that IONP-C/O@LP group presents the highest levels of IL-12p70 and IL-6, suggesting that IONP-C/O@LP can induce the maturation of DCs to upregulate the secretion of proinflammatory cytokines.

IONP have been shown to induce pro-inflammatory macrophage polarization through interferon regulatory factor 5 signaling pathways and directly inhibit tumor growth.[20] The effect of IONP on DCs has not been explored. Because ROS can promote the maturation of iDCs,[21] we hypothesize that IONP may elevate the maturity of DCs through the production of ROS. To

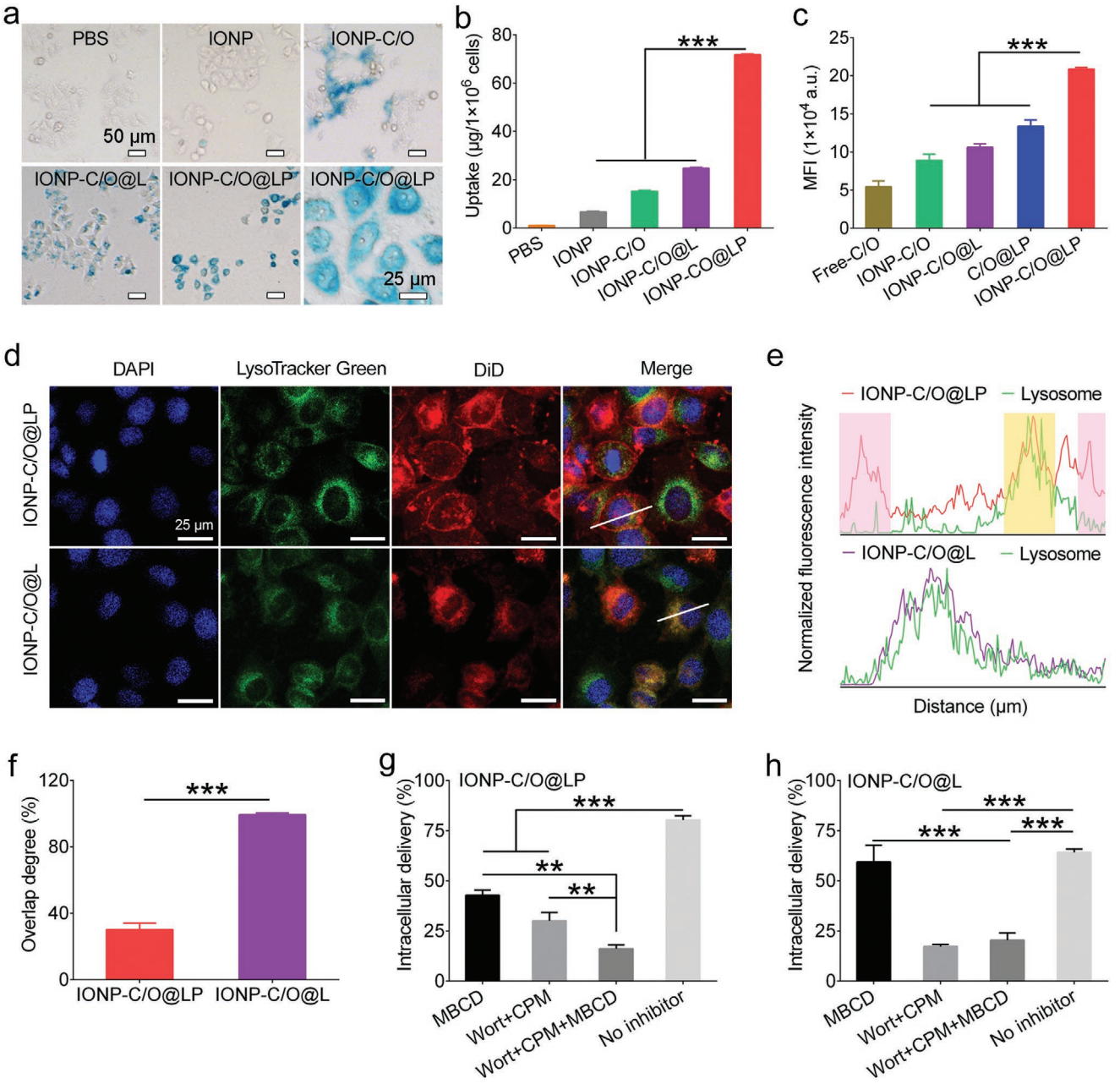

Figure 2. a) Microscopy images of DCs stained with Prussian blue for showing Fe contents in DCs incubated with different nanoformulations. b) Fe contents in DCs treated with different nanoformulations as determined through ICP-MS. Data are shown as mean ± SD ($n = 3$). c) Flow cytometric analysis of Cy5.5-labeled OVAp in DCs incubated with OVAp-contained formulations, respectively. MFI represents mean fluorescence intensity. Data are shown as mean ± SD ($n = 3$). d) Confocal fluorescence images, e) corresponding line scanning analysis, and f) overlap degree of nanoformulations and lysosomes in DC2.4 cells incubated with IONP-C/O@LP. Data are shown as mean ± SD ($n = 3$). g,h) Intracellular delivery of IONP-C/O@LP and IONP-C/O@L after various inhibitor treatments. Data are shown as mean ± SD ($n = 3$). Statistical significance was determined by one-way ANOVA with a Tukey's post hoc test (b, c, g, and h) or Student's *t*-test (f). $^*p < 0.05$, $^{**}p < 0.01$, $^{***}p < 0.001$.

verify this hypothesis, the ROS levels in DCs after incubation with different groups were detected by fluorescent imaging. Apparently, IONP-C/O@LP generate higher ROS signals than C/O@LP, suggesting IONP can increase ROS level in DCs, probably via Fenton reaction.[22] In addition, the increased ROS level positively correlates with the intracellular concentration of IONP, as shown in Figures 2b and 3e, further confirming that IONP is mainly responsible for ROS production in DCs.

2.4. Fluorescence Imaging and MRI of Lymph Nodes In Vivo

The migration of nanovaccine to lymph nodes and their retention largely determine the quality of induced immune responses. To investigate the lymph node accumulation of IONP-C/O@LP, DiD-labeled IONP-C/O@LP were injected to C57BL/6 mice at the tail base, while DiD-labeled IONP-C/O@L and PBS served as negative controls. In vivo imaging

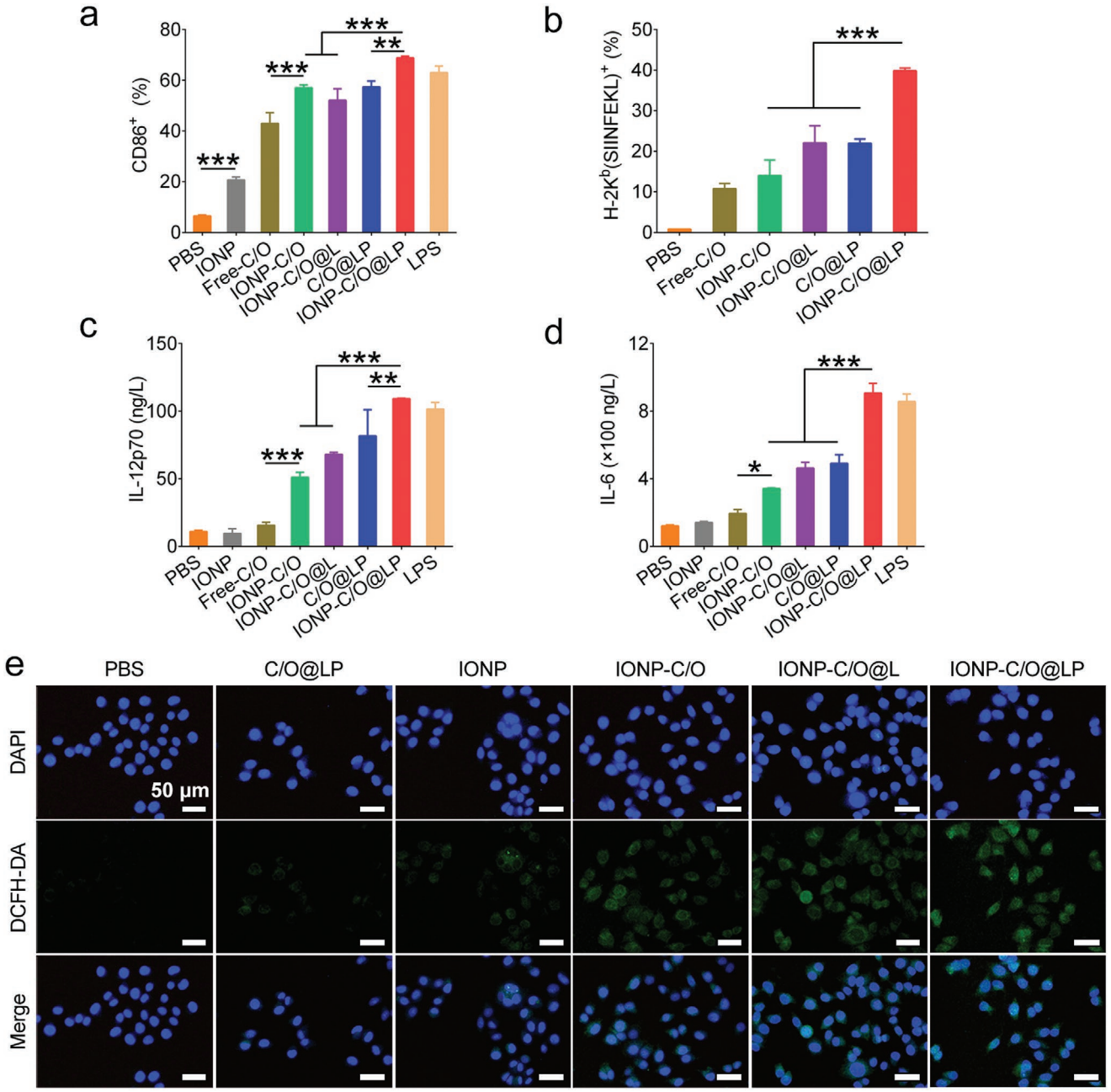

Figure 3. a,b) Flow cytometric analysis on the expressions of $CD86^+$ and $H\text{-}2K^b$ (SIINFEKL) complexes on the surface of DCs to show DC activation and antigen presentation efficiency after incubation with different nanoformulations. Lipopolysaccharide (LPS, a potent TLR4 agonists), which can directly act on DCs and induce DC maturation, was set as the positive control. Data are shown as mean ± SD ($n = 3$). c,d) The secretion levels of IL-12p70 and IL-6 of DCs determined by ELISA assays after incubation with different nanoformulations. Data are shown as mean ± SD ($n = 3$). Statistical significance was determined by one-way ANOVA with a Tukey's post hoc test. $^*p < 0.05$, $^{**}p < 0.01$, $^{***}p < 0.001$. e) Representative fluorescence microscopy images of ROS expressed by DCs after incubation with different nanoformulations. Intracellular ROS was stained by 2′7′-dichlorodihydrofluorescein diacetate (DCFH-DA).

system (IVIS) imaging results in **Figure 4**a show that IONP-C/O@LP get efficiently accumulated in the draining lymph node 48 h post-injection and the accumulation level is ≈15 times higher than that for IONP-C/O@L obtained by quantitatively analyzing ex vivo images of the excised inguinal lymph nodes shown in Figure 4b and Figure S9 (Supporting Information), well consistent with the flow cytometry results, i.e., ≈12 times (Figure 4c and Figure S10a, Supporting Information). Flow cytometry was also used to quantify the cellular uptake of IONP-C/O@LP or IONP-C/O@L by DCs in inguinal lymph nodes. The accumulation level of IONP-C/O@LP in DCs is ≈8 times higher than that for IONP-C/O@L (Figure 4c and Figure S10b, Supporting Information). These results demonstrate that P30 peptide promotes both lymph node accumulation and cellular uptake of IONP-C/O@LP by lymph node DCs.

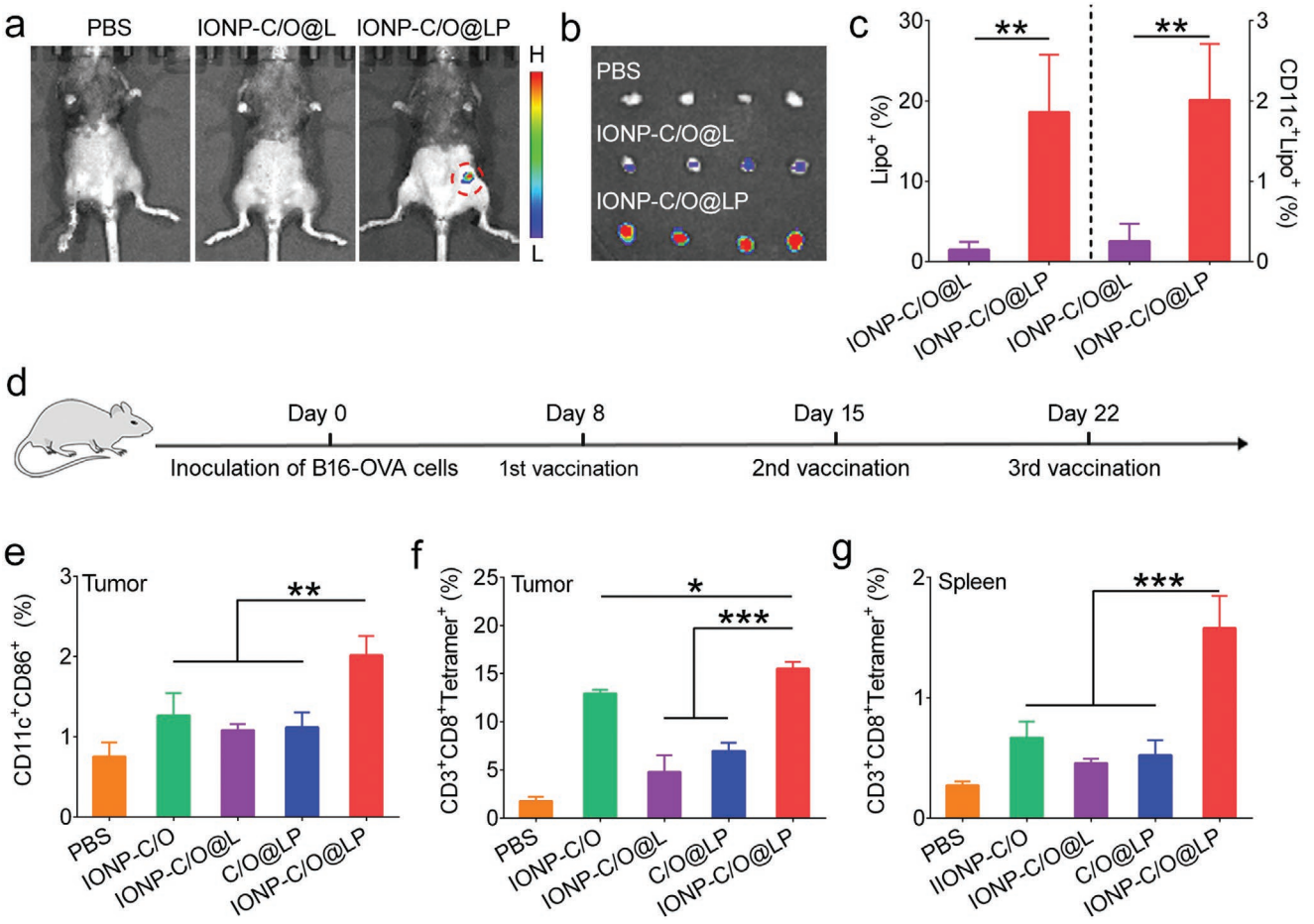

Figure 4. a) The fluorescence images of inguinal lymph node of mice recorded 48 h after the subcutaneous injection of PBS, DiD-labeled IONP-C/O@L, and DiD-labled IONP-C/O@LP at the tail base to show the accumulation of nanovaccine in tumor draining lymph node in vivo. b) An ex vivo fluorescence image of isolated inguinal lymph nodes extracted right after in vivo fluorescence imaging experiments. c) Flow cytometric analysis of the accumulation of DiD-labeled liposome in inguinal lymph node of mice and uptake by lymph node DCs right after the fluorescence imaging. Data are shown as mean ± SD ($n = 4$ biologically independent replicates). Statistical significance was determined by Student's t-test. d) Schematic illustration of the vaccination protocol for subcutaneous B16-OVA melanoma model. e–g) Quantitative analysis on the population of mature DCs and OVAp-specific $CD8^+$ T cells in tumors, and OVAp-specific $CD8^+$ T cells in spleen. Data are shown as mean ± SD ($n = 3$ biologically independent replicates). Statistical significance was determined by one-way ANOVA with a Tukey's post hoc test. $^*p < 0.05$, $^{**}p < 0.01$, $^{***}p < 0.001$.

The IONP offers an opportunity to non-invasively monitor the biodistribution of the nanovaccine through MRI.[23] T_2-weighted MRI images of draining lymph node were obtained before and after footpad injection of IONP-C/O@LP, IONP-C/O, or IONP in mice. The results in Figure S11 (Supporting Information) reveal that IONP-C/O@LP gradually accumulates in draining lymph node over 48 h and shows the highest decrease in T_2 value among all groups. These results are consistent with IVIS data and further demonstrate the superior lymph node accumulation of IONP-C/O@LP.

2.5. Antigen-Specific $CD8^+$ T Cells Induced by Nanovaccines In Vivo

We next studied whether IONP-C/O@LP could trigger the production of antigen-specific T cells in vivo. C57BL/6 mice bearing B16-OVA melanoma xenografts were vaccinated three times at 1-week intervals with various formulations as shown in Figure 4d. The tumor and spleen were collected 24 h after the third immunization for subsequent flow cytometric analysis. The percentages of $CD11c^+CD86^+$ DCs and $CD3^+CD8^+$OVAp-tetramer$^+$ T cells in the tumor of IONP-C/O@LP immunized mice are ≈2.0% and 15.5%, respectively, significantly higher than those for C/O@LP (1.1% and 7.0%), IONP-C/O@L (1.1% and 4.8%), or IONP-C/O (1.3% and 13.0%) groups, as shown in Figure 4e,f and Figure S12a,b (Supporting Information). Additionally, IONP-C/O@LP treatment triggers the highest level of $CD3^+CD8^+$OVAp-tetramer$^+$ T cells in the spleen among all groups (Figure 4g and Figure S12c, Supporting Information). Collectively, these results demonstrate that IONP-C/O@LP elicits strong local and systemic antigen-specific immune responses in vivo.

2.6. Antitumor Effect of the Nanovaccines In Vivo

The therapeutic efficacy of IONP-C/O@LP was evaluated on C57BL/6 mice bearing B16-OVA melanoma xenografts. A total

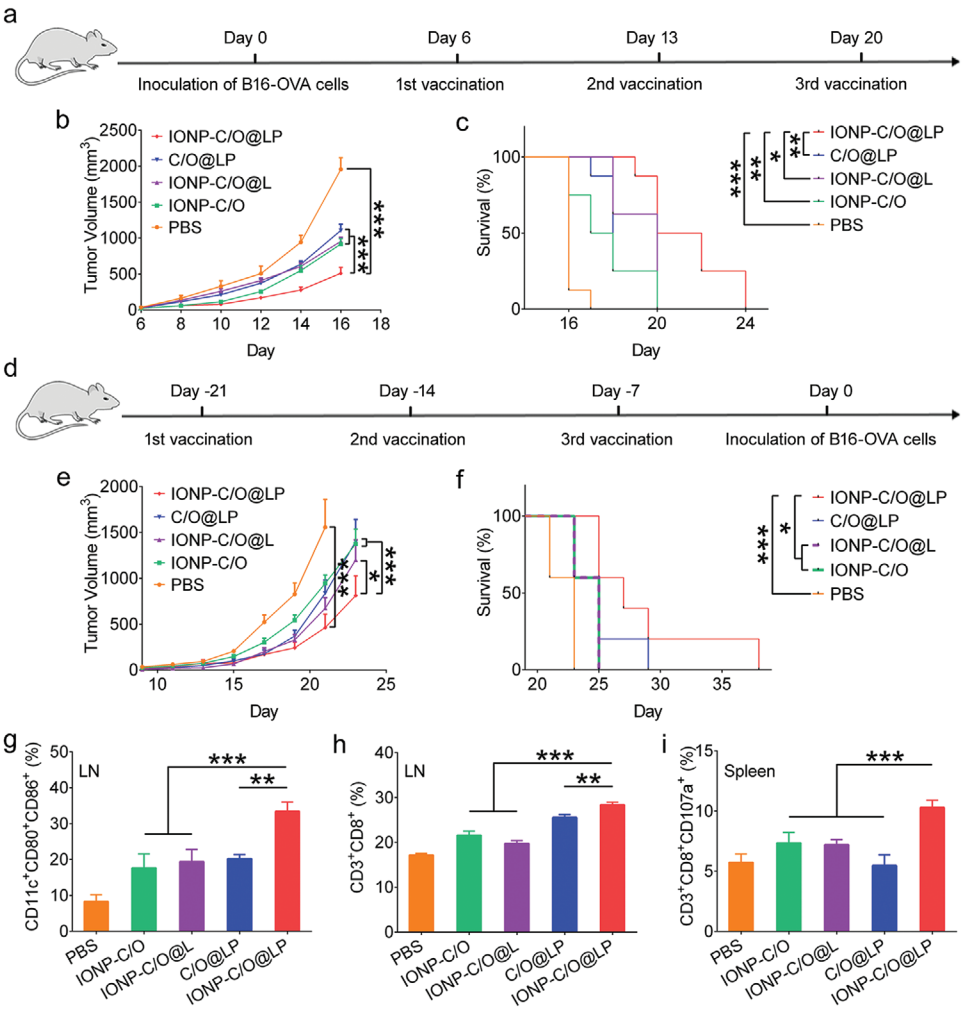

Figure 5. a) Schematic illustration of the immunization schedule for subcutaneous B16-OVA melanoma model. b) Tumor growth curves of B16-OVA melanoma-bearing mice after treatment with different nanoformulations. Data represent mean ± SEM (n = 8 biologically independent replicates). c) Kaplan–Meier survival curves of mice receiving different treatments (n = 8 biologically independent replicates). d) Schematic illustration of prophylactic immunization for subcutaneous B16-OVA melanoma model. e) The tumor growth curves of C57BL/6 mice recorded on day 9 after tumors appeared. Data represent mean ± SEM (n = 5 biologically independent replicates). f) Kaplan–Meier survival curves of mice receiving different treatments (n = 5 biologically independent replicates). Statistical significance of tumor growth curve was determined by two-way ANOVA with a Tukey's post hoc test. Statistical significance of survival curve was determined by Log-rank (Mantel-Cox) test. g–i) Flow cytometric analysis of the population of mature DCs and $CD8^+$ T cells in inguinal lymph node, activated CTLs in spleen from immunized mice. Data are shown as mean ± SD (n = 3, 3, 4 biologically independent replicates, respectively). Statistical significance was determined by one-way ANOVA with a Tukey's post hoc test. *p < 0.05, **p < 0.01, ***p < 0.001.

of 40 mice with tumors of ≈30 mm^3 were randomly divided into five groups (n = 8). These mice were subcutaneously administered at the tail base with PBS, IONP-C/O, IONP-C/O@L, C/O@LP, and IONP-C/O@LP, respectively, on day 6, day 13, and day 20 (**Figure 5**a). Each dose of IONP-C/O@LP contained 21.6 µg of OVAp, 6.9 µg of CpG, and 165.0 µg of Fe in 100 µL PBS. Other control nanoformulations contained the corresponding amounts of OVAp, CpG, and Fe if existed. The results in Figure 5b,c reveal that IONP-C/O@LP significantly inhibit tumor growth and remarkably prolong the animal survival rate compared to PBS, IONP-C/O, IONP-C/O@L, and C/O@LP treatments, suggesting that OVAp, CpG, and IONP work synergistically to enhance the antitumor immune responses. Furthermore, mice in all groups present neglectable fluctuations in body weight (Figure S13, Supporting Information). Hematoxylin and eosin (H&E) staining of major organs show that there are no noticeable inflammations or damages (Figure S14, Supporting Information), indicating insignificant side effects of the nanovaccine in vivo. The H&E staining of tumor tissues show IONP-C/O@LP presents the lowest cell density, the largest intercellular space, and the strongest nucleus atrophy among all groups (Figure S15a, Supporting Information). CD8 marker and IFN-γ were also detected through immunofluorescence assays. From the results of Figures S15b,c and S16 (Supporting Information), the expressions of CD8 and IFN-γ are most significantly upregulated in tumor tissues of mice receiving IONP-C/O@LP, compared with control groups, implying the enhanced infiltration of CTLs in tumor induced by IONP-C/O@LP. Prussian blue staining of Fe contents and immunofluorometric staining of CD8 marker in inguinal

lymph node support that the IONP-C/O@LP accumulate in draining lymph node and enhance the proliferation of $CD8^+$ T cells (Figure S17, Supporting Information).

The prophylactic effects of IONP-C/O@LP were studied using the B16-OVA melanoma model. Twenty-five mice ($n = 5$) were subcutaneously immunized for three times at 1 week interval with IONP-C/O@LP, C/O@LP, IONP-C/O@L, IONP-C/O, and PBS (Figure 5d) before being challenged with B16-OVA melanoma cells. IONP-C/O@LP treated mice show the slowest tumor growth and the longest animal survival period among all groups, as shown in Figure 5e,f. We further explored the relationship of prophylactic effect and systemic immune activation. Lymph nodes and spleen are important secondary lymphoid organs where DCs directly interact with T lymphocytes to induce adaptive immune responses.[24] The population of mature DCs and $CD8^+$ T cells in draining lymph node, and the cytotoxic activity of CTL in spleen were evaluated. C57BL/6 mice were vaccinated three times following the schedule shown in Figure 5d. A week after the third vaccination, the populations of mature DCs and $CD8^+$ T cells in inguinal lymph node were measured by flow cytometry. The population of mature DCs ($CD11c^+CD80^+CD86^+$) in IONP-C/O@LP-treated group is ≈1.7 times that of C/O@LP-treated and IONP-C/O@L-treated groups, and ≈1.9 times of IONP-C/O@L-treated group (Figure 5g). In addition, the amount of $CD8^+$ T cells in tumor draining lymph node of IONP-C/O@LP-treated mice is ≈1.1 times that of C/O@LP, 1.3 times that of IONP-C/O@L, and 1.4 times that of IONP-C/O-treated mice, respectively (Figure 5h), indicating IONP-C/O@LP greatly promote the activation of iDCs and proliferation of $CD8^+$ T cells in tumor draining lymph nodes. The cytotoxicity of $CD8^+$ T cells is reflected by released cytotoxic granules such as perforin and granzymes (a cellular process terms "degranulation") during which the expression of CD107a will be upregulated on the surface of CTLs.[25] To compare the cytotoxic activity of CTLs among different formulations, $CD3^+CD8^+CD107a^+$ T cells in the spleen were evaluated through flow cytometry. IONP-C/O@LP treatment greatly increases the population of $CD3^+CD8^+CD107a^+$ T cells, which is ≈1.9 times that of the C/O@LP, 1.4 times that of IONP-C/O@L and IONP-C/O treatments (Figure 5i). These results suggest that IONP-C/O@LP significantly enhance the cytotoxic activity of CTL in the spleen. Collectively, IONP-C/O@LP trigger both local and systemic antitumor immune responses, therefore holding a great potential to be used as both therapeutic and prophylactic vaccines.

To test the compatibility of the nanovaccine platform with other peptide antigens, $E7_{49\text{-}57}$ peptide (abbreviated as E7p) derived from clinically relevant human papilloma virus 16 (HPV-16), was adopted instead of the model antigen OVAp to construct a new nanovaccine denoted as IONP-C/E@LP following the above design.[26] HPV-16 is a high risk type of HPV, which increases the risk of many kinds of cancers such as cervical, virginal, mouth cancers, etc.[27] E7p has been reported to serve as a promising tumor-specific antigen to prevent and treat HPV-associated cancers.[26] The therapeutic efficacy of IONP-C/E@LP was evaluated in an E7 protein expressing tumor model. TC-1 tumor cells, which were derived from lung epithelial cells of C57BL/6 mice cotransformed with HPV-16 E6 and E7 genes, and c-Ha-*ras* oncogenes were subcutaneously inoculated in C57BL/6 mice. Twenty-four C57BL/6 mice with tumors of ≈30 mm^3 were randomly divided into four groups ($n = 6$). These mice were subcutaneously administered at the tail base with PBS, IONP-C/E@L, C/E@LP, and IONP-C/E@LP, respectively, on day 9, day 16, and day 23 (**Figure 6**a). As shown in Figure 6b, IONP-C/E@LP treatment significantly inhibits tumor growth compared to IONP-C/E@L and C/E@LP groups, suggesting that P30 peptide and IONP both contribute to the enhanced antitumor immune responses. After the third vaccination, the tumor and spleen were collected for flow cytometric analysis. The quantitative data given in Figure 6c,d reveal that the percentages of mature DCs ($CD11c^+CD80^+CD86^+$) and $CD8^+$ T cells in the tumor of IONP-C/E@LP immunized mice are ≈23.5% and 8.1%, respectively, significantly higher than those for C/E@LP (17.5% and 5.2%) and IONP-C/E@L (16.5% and 4.9%) groups. Moreover, the IONP-C/E@LP treatment gives rise to the highest production of CTLs ($CD3^+CD8^+IFN\text{-}\gamma^+$) in the spleen among all groups as shown in Figure 6e. Collectively, these results are consistent with OVA-loaded nanovaccine and demonstrate that IONP-C/E@LP can also elicit strong local and systemic antitumor immune responses in vivo.

To further demonstrate that IONP-C/E@LP trigger the production of antigen-specific T cells, we then evaluated the specificity of cytotoxic T cells through an *ex vivo* killing assay as shown in Figure 6f.[27] Splenocytes from mice vaccinated with IONP-C/E@LP, C/E@LP, IONP-C/E@L, and PBS were collected and restimulated ex vivo by $E7_{49\text{-}57}$ peptide. IONP-C/O@LP (OVAp as antigen) served as a control for evaluating the antigen-specific immune responses. The cytotoxicity of these restimulated splenocytes were measured by incubation with TC-1 tumor cells in vitro. As shown in Figure 6g, the splenocytes from IONP-C/E@LP treated mice show the most potent killing capacity among all groups, which kills ≈44% of TC-1 tumor cells, while splenocytes from C/E@LP and IONP-C/E@L treated mice only kill 24% and 13% of TC-1 tumor cells, respectively. These results further demonstrate that P30 peptide and IONP synergistically improve the CTL responses. Importantly, the splenocytes from IONP-C/O@LP treated mice show nearly the same cytotoxicity to TC-1 cells as those from PBS treated mice, suggesting IONP-C/E@LP can elicit the antigen-specific immune responses. These results demonstrate that our nanovaccine design, as general strategy, is suitable for delivering different peptide antigens.

3. Conclusion

In summary, we report an innovative nanovaccine by encapsulating OVAp and CpG loaded IONPs with DC-targeting lipid film. A two-pronged cellular uptake mechanism is achieved by DC-targeting P30 peptide to deliver OVAp and CpG to cytosol and lysosomes, respectively, so as to maximize the immunological effects of antigen and adjuvant. IONPs in the nanovaccine not only act as carriers for OVAp/CpG and endow the nanovaccine with detectability via MRI, but also exhibit adjuvant effects by generating intracellular ROS. The nanovaccine can efficiently accumulate in tumor draining lymph node and increase the population of mature DCs and $CD8^+$ T cells in tumor draining lymph node. IONP-C/O@LP treatment also increases

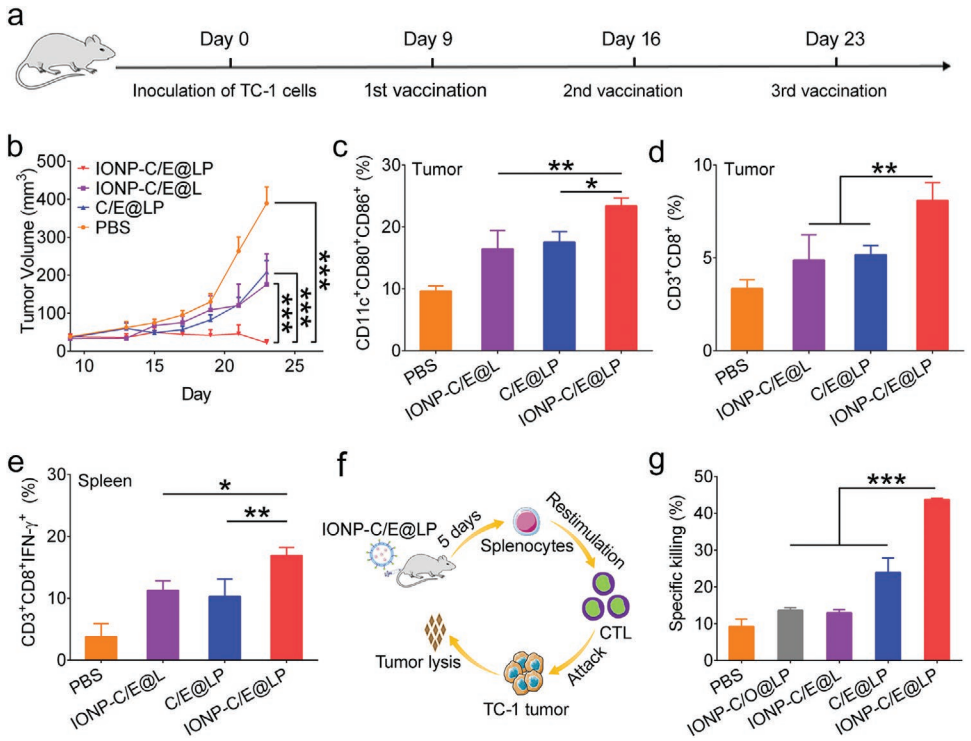

Figure 6. a) Schematic illustration of immunization schedule for subcutaneous TC-1 tumor model. b) Tumor growth curves of TC-1 tumor-bearing mice after treatment with different nanoformulations. Data represent mean ± SEM ($n = 6$ biologically independent replicates). Statistical significance was determined by two-way ANOVA with a Tukey's post hoc test. c–e) Flow cytometric analysis of mature DC and $CD8^+$ T cells in tumor and CTL in spleen ($n = 4, 4, 3$ biologically independent replicates, respectively). Statistical significance was determined by one-way ANOVA with a Tukey's post hoc test. f) Schematic illustration of specific killing assay. g) Specific killing activity of CTLs was measured using a calcein-AM release assay against 5×10^3 calcein-labeled TC-1 tumor cells. The ratio of effector to target cell was 20:1. Data are shown as mean ± SD ($n = 3$ biologically independent replicates). Statistical significance was determined by one-way ANOVA with a Tukey's post hoc test. *$p < 0.05$, **$p < 0.01$, ***$p < 0.001$.

antigen-specific T cells in tumor and spleen, effectively inhibits tumor growth, improves animal survival, and serves as a prophylactic vaccine. These results demonstrate that IONP-C/O@LP elicit potent local, systemic, and antigen-specific antitumor immune responses. The current nanovaccine is superior to solely liposome and inorganic nanoparticle-based systems in terms of efficacy of activating antitumor immune responses. We also demonstrate that this nanovaccine could become a general platform to deliver other peptide antigens. Overall, the present work provides a generic and feasible strategy to efficiently deliver antigens and adjuvants to their corresponding intracellular locations for maximizing the antitumor immune responses.

4. Experimental Section

Materials: The following materials were purchased from Sigma-Aldrich (St. Louis, MO), i.e., ferric chloride hexahydrate, oleic acid, 1-octadecene, LPS, and 4′,6-diamidino-2-phenylindole (DAPI). Cholesterol (CHO), soybean phosphatidylcholine (SPC), and DSPE-PEG-mal were purchased from Aladdin (Shanghai, China). The dip-PEG-mal ligand ($M_w \approx 2000$) was a customized product provided by Beijing Oneder Hightech Co. Ltd. The thiol-modified oligodeoxynucleotide CpG (5′-tccatgacgttcctgacgtt-3′) was a customized product provided by BGI Genomics Co. Ltd (Shenzhen, China). Cysteine-contained $OVA_{257\text{-}264}$ (SIINFEKLC), FITC-labeled $OVA_{257\text{-}264}$, Cy5.5-labeled $OVA_{257\text{-}264}$ were a customized product provided by Top-peptide Biotechnology Co. Ltd. (Shanghai, China). Thiol-modified P30 peptide (C-CGRWSGWPADLC) and cysteine-contained $E7_{49\text{-}57}$ (RAHYNIVTFC) were a customized product provided by GL Biochem Ltd. (Shanghai, China). The anti-mouse CD16/32 antibody, FITC-labeled anti-mouse CD80 antibody, phycoerythrin (PE)-labeled anti-mouse CD86 antibody, allophycocyanin (APC)-labeled anti-mouse CD86 antibody, APC-labeled anti-mouse H-$2K^b$ bound to SIINFEKL (H-$2K^b$ (SIINFEKL)) antibody, PE-labeled anti-mouse CD11c antibody, FITC-labeled anti-mouse CD3 antibody, peridinin-chlorophyll-protein complex/cyanine 5.5 (PerCP/Cy5.5)-labeled anti-mouse CD8a antibody, Brilliant Violet 421 (BV421)-labeled anti-mouse CD107a antibody, mouse IL-12p70 ELISA kit, and mouse IL-6 ELISA kit were purchased from Dakewe Biotech Co., Ltd. (Shenzhen, China). APC-labeled anti-mouse H-$2K^b$/SIINFEKL tetramer, FITC-labeled CD8a antibody, violetFluor 450 (V450)-labeled CD3 antibody were purchased from MBL Co., Ltd. (Japan). DCFH-DA, MTT, LysoTracker Green, DiD dye were purchased from AAT Bioquest. Calcein-AM dye, Triton X-100 and interleukin 2 (IL-2) were purchased from Solarbio. Advanced Dulbecco's Modified Eagle's Medium (DMEM) medium and FBS were obtained from Gibco (Beijing, China). Analytical grade chemical reagents such as ethanol, cyclohexane, and tetrahydrofuran were purchased from Sinopharm Chemical Reagent Beijing, Co. Ltd. Milli-Q purified water (18.2 MΩ cm) was used for all experiments. The DC2.4 (murine bone marrow dendritic cell line) and TC-1 (mouse lung epithelial cell line cotransformed with HPV16 E6 and E7 genes, and c-Ha-*ras* oncogenes) were purchased from American Type Culture Collection. OVA-transfected B16 melanoma cell line (B16-OVA) was obtained from State Key Laboratory of Radiation Medicine and Protection, Soochow University.

Preparation of IONP-C/O Conjugates: The PEGylated Fe_3O_4 nanoparticles were synthesized according to a previous work.[12] Thiol-modified CpG (0.64 mg, 0.1 μmol) in water (1 mL) was introduced to

6 mL aqueous solution containing 12.24 mg of IONPs. After stirring at room temperature for 2 h, the resulting product was purified through ultrafiltration with PBS for three cycles using 30 kDa MWCO centrifugal filter (Millipore YM-30), and then the CpG concentration in filtrates were measured through NanoDrop One microvolume ultraviolet and visible (UV–vis) spectrophotometer. After that, OVAp (2.44 mg, 2.5 µmol) in water (2 mL) was added to react with the as-prepared IONP-CpG conjugates for 2 h at the same reaction conditions, followed by the same post-treatment procedures to obtain IONP-C/O conjugates, the uncoupled peptides in filtrates were determined by UV–vis absorption spectroscopy on a Cary 50 UV–vis spectrometer at room temperature.

Synthesis of DSPE-PEG-P30: Thiolated P30 peptide was covalently connected to maleimide-modified DSPE-PEG-mal through click reaction.[29] Typically, P30 peptide and DSPE-PEG-mal were mixed at a molar ratio of 2:1 in the mixture of water and methanol. The reaction mixture was moderately stirred at room temperature for 2 h in darkness. After that, unreacted P30 was removed through dialysis against distilled H_2O for 48 h (MWCO = 3500 Da). The final solution was lyophilized and characterized by MALDI-TOF-MS.

Preparation of IONP-C/O@LP: IONP-C/O@LP were prepared by a conventional film hydration method.[14] SPC, CHO, and DSPE-PEG-P30 were dissolved in chloroform at a mass ratio of 10:6:1. The organic solvent was then evaporated by rotating evaporation at 45 °C, and a homogeneous dry lipid film was obtained by being dried in vacuum for 24 h. After that, 12 mg of IONP-C/O was dispersed in 4 mL PBS for hydrating the dry lipid film at room temperature. The resulting coarse liposome suspension was further processed by probe sonication (200 W, on 5 s, off 5 s, 10 min in total). After that, the liposome suspension was sequentially extruded through polycarbonate membrane with a pore size of 450, 220, and 100 nm to control the size of IONP-C/O@LP. The liposome suspension was centrifuged at the speed of 8000 rpm for 10 min at 4 °C to remove the unencapsulated IONP-C/O conjugates. The encapsulation efficiency was calculated as $W_{en}/W_{origin} \times 100\%$, where W_{en} is the amount of IONP-C/O conjugates (the gross weight of IONPs, OVAp, and CpG) encapsulated in liposome and W_{origin} is the original amount of IONP-C/O conjugates. The obtained IONP-C/O@LP liposomes were treated with methanol and the iron concentration in IONP-C/O conjugates was determined by 1,10-phenanthroline photometric method after eroding with concentrated hydrochloric acid.

Characterization of Different Nanoformulations: TEM images of IONP, IONP-C/O, and IONP-C/O@LP particles were taken on a HT-7700 transmission electron microscope operating at an acceleration voltage of 100 kV. SEM images of IONP-C/O@LP particles were taken on an S-4800 scanning electron microscope operating at an acceleration voltage of 10 kV. The particle size of IONP and IONP-C/O was determined by counting at least 300 nanoparticles per sample. The respective hydrodynamic size and zeta potential of IONP, IONP-C/O, IONP-C/O@L, C/O@LP and IONP-C/O@LP nanoparticles were determined by DLS using a Nano Zetasizer (Malvern) equipped with a solid state He-Ne laser ($\lambda = 632.8$ nm) at 298 K. The colloidal stability of IONP-C/O@LP in PBS with 10% FBS was evaluated by DLS, monitoring for 6 d at 4 °C.

Cell Culture: For in vitro cell experiments, DC2.4 cells were firstly seeded in plates and cultured in a medium of DMEM supplemented with 10% FBS and 1% penicillin-streptomycin for 24 h at 37 °C under an atmosphere of 5% carbon dioxide to ensure a firm adherence. The corresponding cell densities seeded in plates for different experiments were given as follows: 1×10^5 cells/well for 12-well plates, 1×10^6 cells/well for six-well plates, and 1×10^4 cells/well for 96-well plates.

Cellular Uptake Studies In Vitro: DC2.4 cells seeded in six-well plates were incubated for 12 h with IONP-C/O@LP (containing 1.5 mg of lipid, 150 µg of Fe, 19.5 µg of OVAp, and 6 µg of CpG in 3 mL DMEM) and control nanoformulations. After that, the cells were fixed with 4% paraformaldehyde and then stained with Prussian blue for Fe staining. The fluorescence imaging of the resulting cells was carried out on an inverted fluorescence microscope (Olympus X71). After imaging, the cells were collected and digested for ICP-MS measurements to determine iron concentration in cells. To determine the intracellular delivery efficacy, DC2.4 cells cultured in 12-well plates were incubated with formulations containing Cy5.5-labeled OVAp for 12 h. Then the cells were collected for flow cytometric analysis (BD Acurri C6, USA). 10 000 events were collected and analyzed through Flowjo 7.6.1 software.

The Intracellular Delivery of IONP-C/O@LP In Vitro: To observe the internalization process of IONP-C/O@LP, DiD-labeled nanovaccines (containing 1 mg of lipid, 100 µg of Fe, 13 µg of OVAp, 6 µg of CpG in 2 mL DMEM) were added gently into 12-well plates seeded with DC2.4 cells and IONP-C/O@L particles were designed as control. After incubation for 6 h at 37 °C, LysoTracker Green was used to identify the lysosomes. And DAPI was used to identify cell nuclei after being fixed. Confocal laser scanning microscopy studies were carried out using LSM 5 EXCITER (Carl Zeiss Co. Ltd.). Colocalization analysis was performed with LSM Software ZEN 2009 and Image J.

To determine the internalization pathways of IONP-C/O@LP, membrane fusion and endocytic inhibitors were used to block the nanovaccine delivery. DC2.4 cells cultured in 12-well plates were pretreated with methyl-β-cyclodextrin (12.5 mg mL^{-1}), wortmannin (450 ng mL^{-1}), and chlorpromazine (4.5 µg mL^{-1}), or all three inhibitors in DMEM for 1 h at 37 °C and 5% CO_2. Then the inhibitor-treated cells were treated with IONP-C/O@LP or IONP-C/O@L containing FITC-labeled OVAp for 6 h. The cells were analyzed with flow cytometer (BD Acurri C6, USA). 10 000 events were collected and analyzed through Flowjo 7.6.1 software.

Cytotoxicity Assessment for IONP-C/O@LP: DC2.4 cells seeded in 96-well plates were incubated with IONP-C/O@LP and control nanoformulations for 24 h at a series of concentrations (0, 1, 10, 50, 100, 200 µg Fe mL^{-1}), respectively. After incubated in culture medium for another 48 h, MTT (0.5 mg mL^{-1}, 100 µL) was added for 4 h. The supernatant was carefully removed and 100 µL dimethyl sulfoxide was added to each well to dissolve the crystal products. The absorbance of each well at 490 nm was then recorded on a microplate reader (Thermo, Varioskan Flash), while the optical density at 630 nm was used as reference. the PBS control group was supposed to have 100% cell viability.

Maturity Level of DCs upon Stimulation with Nanovaccines In Vitro: DC2.4 cells seeded in six-well plates were treated with IONP-C/O@LP and control nanoformulations, respectively. After coincubation for 12 h, the incubation media were collected for quantitatively analyzing the secretion levels of interleukin IL-12p70 and IL-6 through cytokine-specific ELISA kits, and the obtained DC2.4 cells were collected using cell scrapers. The DC 2.4 cells were preincubated with anti-mouse CD16/CD32 antibody. Then the DC 2.4 cells were stained with PE-labeled CD86 antibody for 30 min on ice. The DC cell surface expression levels of CD86 were analyzed by flow cytometer (BD Acurri C6, USA) and 10 000 events of the stained cells were analyzed. To detect antigen presentation, the cells were stained with APC-labeled H-2K^b(SIINFEKL) antibody. The data were analyzed by Flowjo 7.6.1 software.

Detection of Intracellular ROS Level In Vitro: DC2.4 cells seeded in 12-well plates were treated with IONP-C/O@LP for 12 h at the concentration of 50 µg Fe mL^{-1} and control nanoformulations, respectively. Then the cells were collected and stained with DCFH-DA (1×10^{-3} M) for 15 min for ROS detection. After being fixed with 4% paraformaldehyde, the cells were stained with DAPI for 10 min. The intracellular levels of ROS were studied with fluorescence microscopy (Eclipse 80i; Nikon, Japan). The excitation was set at 488 nm and the fluorescence signals were collected through a window between 500 and 560 nm.

Imaging Tumor Draining Lymph Nodes In Vivo: The imaging studies were implemented on C57BL/6 mice. Twelve C57BL/6 mice were randomly divided into three groups (n = 4) and subcutaneously injected at the tail base with 100 µL DiD-labeled IONP-C/O@LP or DiD-labeled IONP-C/O@L. PBS was used as a blank control. After 48 h, the mice were imaged by IVIS Lumina III in vivo Imaging System (Ex/Em = 640/680 nm, Perkin Elmer, USA), and then sacrificed for extracting the inguinal lymph node at the right side of mice for ex vivo imaging. Right after the fluorescence imaging, the inguinal lymph nodes were digested to single-cell suspensions for flow cytometry.

PE anti-CD11c antibody was used to stain DCs in lymph node by flow cytometric analysis. 10 000 events were collected and data were analyzed through cytoExpert software.

Regarding MRI of the lymph nodes, mice were injected with 50 µL IONP-C/O@LP under anesthesia. IONP-C/O and IONP were used as controls. The MR images were acquired on a 7.0 T Bruker Biospec animal MRI instrument at designed time points post-injection. The detailed T_2 imaging parameters were given as follows: FoV (field of view) = 3.5 × 3.5 cm^2, matrix size = 200 × 200, slice thickness = 1 mm, TE = 40 ms, TR = 3000 ms, and NEX = 3. The mice were anesthetized with 1.5% isoflurane delivered via nose cone during the imaging process.

Animal Tumor Model: The animal tumor models were established upon subcutaneous injections of B16-OVA melanoma cells (≈5 × 10^5) or TC-1 tumor cells (≈5 × 10^5) into six-week-old female C57BL/6 mice at the flank region of the right hind legs. The tumor therapeutic and prophylactic experiments were carried out by subcutaneously injection at the tail base with different nanoformulations, respectively. The tumor volume and mice weight were recorded when tumors reached ≈30 mm^3. The experimental endpoint was defined as either death or a tumor size greater than 1500 mm^3.

In Vivo Detection of Antigen-Specific CD8$^+$ T Cells in Tumor and Spleen: Twenty C57BL/6 mice bearing B16-OVA melanoma xenografts were randomized into five groups (n = 4) and vaccinated for three times at one-week interval with 100 µL IONP-C/O@LP (contain 21.6 µg of OVAp, 6.9 µg of CpG, and 165.0 µg of Fe). IONP-C/O, IONP-C/O@L, C/O@LP, and PBS were used as controls. 24 h after the last vaccination, spleens and tumors of mice were collected and digested to single-cell suspensions for flow cytometry. After incubation with anti-CD16/32 antibody, the cell suspensions were stained with APC H-2K^b/SIINFEKL tetramer, FITC anti-CD8a antibody, and V450 anti-CD3 antibody for flow cytometric analysis. 100 000 events were collected and analyzed through cytoExpert software. Moreover, another part of tumor cell suspension was incubated with PE anti-CD11c antibody and APC anti-CD86 antibody for mature DC staining and followed the same procedures of flow cytometric analysis.

Tumor Inhibition against B16-OVA Melanoma Model: Forty B16-OVA melanoma-bearing C57BL/6 mice were randomly divided into five groups (n = 8). Mice were vaccinated for three times. The tumor size and mice weight were measured every 2 d and the tumor volume (V) was calculated according to $V = (a \times b^2)/2$, where a and b represent the length and width of the tumor, respectively. After day 16, mice in each group were fed for calculating the survival rates.

Twenty B16-OVA melanoma-bearing C57BL/6 mice were randomly divided into four groups (n = 5). Mice were injected once a week for three times with 100 µL IONP-C/O@LP and IONP-C/O, C/O@LP, and PBS (contain 21.6 µg OVAp, 6.9 µg CpG, and 165.0 µg Fe if exists). Seven days after the third vaccination, mice were sacrificed and the tumor tissues, inguinal lymph nodes at the tumor site, and major organs of mice were extracted and fixed in 4% paraformaldehyde for histopathological and immunohistochemical analysis by Servicebio (Wuhan, China). Three adjacent slices of tumor tissues were chosen for H&E staining, CD8, and IFN-γ immunofluorescence assays. In the same way, slices of inguinal lymph nodes were obtained for Prussian blue staining and CD8 immunofluorescence assays. The major organs, including spleen, heart, liver, lung, and kidney, were obtained for histopathological analysis through H&E staining.

Tumor Prevention against B16-OVA Melanoma Model and Flow Cytometric Analysis: Twenty-five C57BL/6 mice were randomly divided into five groups (n = 5) and vaccinated for three times. Then on day 0, they were inoculated with 5 × 10^5 B16-OVA melanoma cells at the blank region of mouse right hinder legs. The tumor size of mice was observed every 2 d. After day 21, mice in each group were fed for calculating the survival rates.

Twenty C57BL/6 mice were randomized into five groups (n = 4) and vaccinated for three times. Seven days after the last vaccination, the inguinal lymph nodes and spleens of mice were harvested and digested to single-cell suspensions for flow cytometric analysis. After incubation with anti-CD16/CD32 antibody, the cells from inguinal lymph nodes were stained with PE anti-CD11c antibody, FITC anti-CD80 antibody, and PerCP/Cy5.5 anti-CD86 antibody to analyze matured DCs, or FITC anti-CD3 antibody and APC anti-CD8 antibody for CD8$^+$ T cells. Cells from spleens were incubated with 10 µg mL^{-1} $OVA_{257-264}$ peptide and 10 ng mL^{-1} IL-2 for 60 h to evaluate the antigen-specific CTL responses restimulated by the same antigen. After restimulation, the splenocytes were stained with FITC anti-CD3 antibody, PerCP/Cy5.5 anti-CD8 antibody, BV421 anti-CD107a antibody for activated CTLs analyzed by flow cytometry. 10 000 events were collected and analyzed through cytoExpert software.

Tumor Inhibition against TC-1 Tumor Model and Flow Cytometric Analysis: Twenty-four TC-1 tumor-bearing C57BL/6 mice were randomly divided into four groups (n = 6). Mice were vaccinated for three times with 100 µL of IONP-C/E@LP, C/E@LP, IONP-C/E@L, and PBS. The tumor size was recorded every 2 d. One day after the last vaccination, the single-cell suspensions of tumor tissues of mice were stained with PE anti-CD11c antibody, FITC anti-CD80, and APC anti-CD86 antibody for mature DCs, or FITC anti-CD3 antibody and APC anti-CD8 antibody for CD8$^+$ T cells for flow cytometry analysis. Cells from spleens were incubated with 10 µg mL^{-1} $E7_{49-57}$ peptide for 6 h. 5 µg mL^{-1} of brefeldin A was added for the last 3 h. After restimulation, the splenocytes were collected and then stained with FITC anti-CD3 antibody, APC anti-CD8 antibody, PE anti-IFN-γ antibody for flow cytometric analysis. 10 000 events were collected and analyzed through cytoExpert software.

E7p Antigen-Specific Killing Assay: The specific killing assay was performed using a calcein-AM release assay as previously described.[28] Fifteen C57BL/6 mice were randomly divided into five groups (n = 3) and vaccinated once. The splenocytes were harvested 5 d after vaccination and cultured for 60 h in DMEM containing 10 µg mL^{-1} of $E7_{49-57}$ peptide and 10 ng mL^{-1} of IL-2 (or 10 µg mL^{-1} of $OVA_{257-264}$ peptide and 10 ng mL^{-1} of IL-2 for IONP-C/O@LP treated group). TC-1 tumor cells were labeled with 15 × 10^{-6} M calcein-AM at 37 °C for 30 min under dark condition. After washing for three times, TC-1 cells were plated into round-bottom 96-well plates at a concentration of 5 × 10^3 cells per well. Restimulated splenocytes were added to TC-1 cells at various effector/target cell ratios (E:T) of 50:1, 20:1, 5:1, and 1:1 in quadruplicate. Free TC-1 cells were used as blanks (spontaneous-release wells). Lysis buffer (medium plus 2% Triton X-100) was added to TC-1 cells to fully release the calcein dye (the maximum-release wells). After coincubation for 4 h, 75 µL of each supernatant was transferred to black 96-well plates and read on a microplate reader (BioTek, Synergy H1) with excitation at 485 nm and emission at 538 nm. Specific killing was calculated by the following equation [(test release − spontaneous release)/(maximum release − spontaneous release)] × 100%. The optimum E:T ratio in this experiment was determined to be 20:1.

The synthesis of nanovaccine was repeated at least three times. The in vitro experiments were repeated at least twice with three technical replicates per group. The in vivo fluorescence imaging and flow cytometric analysis of mice without tumors were performed twice with three to four biologically independent replicates per group. Tumor inhibition study in the B16-OVA melanoma model was performed twice with five to eight biologically independent replicates per group. Tumor inhibition study was repeated in the TC-1 tumor model with six biologically independent replicates per group. The flow cytometric analysis of immune cells in tumor and spleen was performed in the B16-OVA melanoma model and was repeated in the TC-1 tumor model with three or four biologically independent replicates per group.

Statistical Analysis: Statistical analysis was performed in Graphpad Prism 6.01. Technical replicates were used in all experiments unless otherwise stated. Student's t-test was adopted when only two value sets were compared, while one-way ANOVA with a Tukey's post hoc test was used for multiple comparisons. The statistical differences of tumor growth over time (two variables) were calculated by two-way ANOVA with a Tukey's post hoc test. The analysis of statistical significance on survival rate adopts Log-rank (Mantel-Cox) test. The specific statistical methods are indicated in the figure legends. All tests were bilateral, and $*p < 0.05$ was considered significant, and $**p < 0.01$ and $***p < 0.001$ were considered highly significant. Data were presented as mean ± standard

deviation (SD) or mean ± standard error of mean (SEM) as indicated in the figure legends.

All animals were housed under specific pathogen free (SPF) conditions in Department of Laboratory Animal Science, Peking University Health Science Center. All animal experiments reported here were performed according to a protocol approved by the Peking University Institutional Animal Care and Use Committee. The assigned accreditation number of the investigator is 1119030800103.

Supporting Information

Supporting Information is available from the Wiley Online Library or from the author.

Acknowledgements

J.M. and P.Z. contributed equally to this work. The authors acknowledge the financial support from the National Key Research and Development Program of China (2018YFA0208800), National Natural Science Foundation of China (NSFC) (81720108024, 81530057, 81801766, 81671754, 22177115), CAS-VPST Silk Road Science Fund 2019 (GJHZ201963), the Youth Innovation Promotion Association CAS (2018042), and UNSW-CAS collaborative research grant.

Conflict of Interest

The authors declare no conflict of interest.

Data Availability Statement

The data that support the findings of this study are available from the corresponding author upon reasonable request.

Keywords

cancer immunotherapy, CpG, iron oxide nanoparticles, membrane fusion, nanovaccines

Received: March 8, 2022
Revised: March 22, 2022
Published online:

[1] a) Y. Zhang, S. Lin, X.-Y. Wang, G. Zhu, *Wiley Interdiscip. Rev.: Nanomed. Nanobiotechnol.* **2019**, *11*, e1559; b) S. J. Yu, C. Wang, J. C. Yu, J. Q. Wang, Y. Lu, Y. Q. Zhang, X. D. Zhang, Q. Y. Hu, W. J. Sun, C. L. He, X. S. Chen, Z. Gu, *Adv. Mater.* **2018**, *30*, 1801527; c) Y. P. He, C. Hong, J. H. Li, M. T. Howard, Y. Z. Li, M. E. Turvey, D. Uppu, J. R. Martin, K. T. Zhang, D. J. Irvine, P. T. Hammond, *ACS Nano* **2018**, *12*, 10272; d) S. Y. Neshat, S. Y. Tzeng, J. J. Green, *Curr. Opin. Biotechnol.* **2020**, *66*, 1.

[2] a) S. K. Wculek, F. J. Cueto, A. M. Mujal, I. Melero, M. F. Krummel, D. Sancho, *Nat. Rev. Immunol.* **2020**, *20*, 7; b) D. J. Irvine, M. C. Hanson, K. Rakhra, T. Tokatlian, *Chem. Rev.* **2015**, *115*, 11109.

[3] a) H. Wang, D. J. Mooney, *Nat. Mater.* **2018**, *17*, 761; b) F. Li, W. Nie, F. Zhang, G. Lu, C. Lv, Y. Lv, W. Bao, L. Zhang, S. Wang, X. Gao, W. Wei, H.-Y. Xie, *ACS Cent. Sci.* **2019**, *5*, 796.

[4] a) K. L. Rock, L. Shen, *Immunol. Rev.* **2005**, *207*, 166; b) P. Cresswell, A. L. Ackerman, A. Giodini, D. R. Peaper, P. A. Wearsch, *Immunol. Rev.* **2005**, *207*, 145; c) O. Met, S. Buus, M. H. Claesson, *Cell. Immunol.* **2003**, *222*, 126.

[5] a) E. Latz, A. Schoenemeyer, A. Visintin, K. A. Fitzgerald, B. G. Monks, C. F. Knetter, E. Lien, N. J. Nilsen, T. Espevik, D. T. Golenbock, *Nat. Immunol.* **2004**, *5*, 190; b) S. Akira, K. Takeda, *Nat. Rev. Immunol.* **2004**, *4*, 499; c) C. Bode, G. Zhao, F. Steinhagen, T. Kinjo, D. M. Klinman, *Expert Rev. Vaccines* **2011**, *10*, 499.

[6] a) M. S. Goldberg, *Cell* **2015**, *161*, 201; b) C. Zhang, K. Y. Pu, *Chem. Soc. Rev.* **2020**, *49*, 4234; c) R. Kuai, L. J. Ochyl, K. S. Bahjat, A. Schwendeman, J. J. Moon, *Nat. Mater.* **2017**, *16*, 489; d) J. Xu, Q. Ma, Y. Zhang, Z. Fei, Y. Sun, Q. Fan, B. Liu, J. Bai, Y. Yu, J. Chu, J. Chen, C. Wang, *Nat. Commun.* **2022**, *13*, 110.

[7] a) W. Q. Li, X. F. Zhang, C. X. Zhang, J. Y. Yan, X. C. Hou, S. Du, C. X. Zeng, W. Y. Zhao, B. B. Deng, D. W. McComb, Y. B. Zhang, D. D. Kang, J. N. Li, W. E. Carson, Y. Z. Dong, *Nat. Commun.* **2021**, *12*, 7264; b) S. T. Reddy, M. A. Swartz, J. A. Hubbell, *Trends Immunol.* **2006**, *27*, 573; c) R. A. Meyer, J. C. Sunshine, J. J. Green, *Trends Biotechnol.* **2015**, *33*, 514.

[8] a) L. Luo, M. Z. Iqbal, C. Liu, J. Xing, O. U. Akakuru, Q. Fang, Z. Li, Y. Dai, A. Li, Y. Guan, A. Wu, *Biomaterials* **2019**, *223*, 119464; b) D. A. Giljohann, D. S. Seferos, W. L. Daniel, M. D. Massich, P. C. Patel, C. A. Mirkin, *Angew. Chem., Int. Ed.* **2010**, *49*, 3280; c) L. J. Shen, L. J. Sigal, M. Boes, K. L. Rock, *Immunity* **2004**, *21*, 155.

[9] a) Q. Zhou, Y. Zhang, J. Du, Y. Li, Y. Zhou, Q. Fu, J. Zhang, X. Wang, L. Zhan, *ACS Nano* **2016**, *10*, 2678; b) C. Lai, S. Duan, F. Ye, X. Hou, X. Li, J. Zhao, X. Yu, Z. Hu, Z. Tang, F. Mo, X. Yang, X. Lu, *Theranostics* **2018**, *8*, 1723.

[10] M. P. Stewart, A. Sharei, X. Y. Ding, G. Sahay, R. Langer, K. F. Jensen, *Nature* **2016**, *538*, 183.

[11] a) B. Kim, S. Sun, J. A. Varner, S. B. Howell, E. Ruoslahti, M. J. Sailor, *Adv. Mater.* **2019**, *31*, 1902952; b) J. Zhou, Z. Shao, J. Liu, Q. Duan, X. Wang, J. Li, H. Yang, *ACS Appl. Bio Mater.* **2020**, *3*, 2686; c) C. Shi, M. L. Li, Z. Zhang, Q. C. Yao, K. Shao, F. Xu, N. Xu, H. D. Li, J. L. Fan, W. Sun, J. J. Du, S. Long, J. Y. Wang, X. J. Peng, *Biomaterials* **2020**, *233*, 119755.

[12] Z. Gao, Y. Hou, J. Zeng, L. Chen, C. Liu, W. Yang, M. Gao, *Adv. Mater.* **2017**, *29*, 1701095.

[13] a) A. Faham, J. G. Altin, *Int. J. Cancer* **2011**, *129*, 1391; b) C. Frick, A. Odermatt, K. Zen, K. J. Mandell, H. Edens, R. Portmann, L. Mazzucchelli, D. L. Jaye, C. A. Parkos, *Eur. J. Immunol.* **2005**, *35*, 3610.

[14] a) M. N. Hossen, L. Wang, H. R. Chinthalapally, J. D. Robertson, K. M. Fung, S. Wilhelm, M. Bieniasz, R. Bhattacharya, P. Mukherjee, *Sci. Adv.* **2020**, *6*, eaba5379; b) P. B. Santhosh, S. I. Kiryakova, J. L. Genova, N. P. Ulrih, *Colloids Surf., A* **2014**, *460*, 248.

[15] H.-L. Xu, J.-J. Yang, D.-L. Zhuge, M.-T. Lin, Q.-Y. Zhu, B.-H. Jin, M.-Q. Tong, B.-X. Shen, J. Xiao, Y.-Z. Zhao, *Adv. Healthcare Mater.* **2018**, *7*, 1701130.

[16] J. V. Jokerst, T. Lobovkina, R. N. Zare, S. S. Gambhir, *Nanomedicine* **2011**, *6*, 715.

[17] R. Mout, M. Ray, G. Y. Tonga, Y. W. Lee, T. Tay, K. Sasaki, V. M. Rotello, *ACS Nano* **2017**, *11*, 2452.

[18] A. V. Kroll, R. H. Fang, Y. Jiang, J. Zhou, X. Wei, C. L. Yu, J. Gao, B. T. Luk, D. Dehaini, W. Gao, L. Zhang, *Adv. Mater.* **2017**, *29*, 1703969.

[19] R. Yang, J. Xu, L. Xu, X. Sun, Q. Chen, Y. Zhao, R. Peng, Z. Liu, *ACS Nano* **2018**, *12*, 5121.

[20] a) S. Zanganeh, G. Hutter, R. Spitler, O. Lenkov, M. Mahmoudi, A. Shaw, J. S. Pajarinen, H. Nejadnik, S. Goodman, M. Moseley, L. M. Coussens, H. E. Daldrup-Link, *Nat. Nanotechnol.* **2016**, *11*, 986; b) Z. Gu, T. Liu, J. Tang, Y. Yang, H. Song, Z. K. Tuong, J. Fu, C. Yu, *J. Am. Chem. Soc.* **2019**, *141*, 6122.

[21] a) S. Kantengwa, L. Jornot, C. Devenoges, L. P. Nicod, *Am J. Respir. Crit. Care Med.* **2003**, *167*, 431; b) V. Verhasselt, M. Goldman, F. Willems, *Eur. J. Immunol.* **1998**, *28*, 3886; c) K. Rutault, C. Alderman, B. M. Chain, D. R. Katz, *Free Radical Biol. Med.* **1999**, *26*, 232.

[22] a) B. Yang, Y. Chen, J. Shi, *Adv. Mater.* **2019**, *31*, 1901778; b) Y. Du, C. Yang, F. Y. Li, H. W. Liao, Z. Chen, P. H. Lin, N. Wang, Y. Zhou, J. Y. Lee, Q. Ding, D. S. Ling, *Small* **2020**, *16*, 2002537; c) Z. B. Cao, B. Li, L. Y. Sun, L. Li, Z. P. Xu, Z. Gu, *Small Methods* **2020**, *4*, 1900343.

[23] a) A. Pardo, B. Pelaz, J. Gallo, M. Banobre-Lopez, W. J. Parak, S. Barbosa, P. del Pino, P. Taboada, *Chem. Mater.* **2020**, *32*, 2220; b) B. Liu, C. X. Li, G. Y. Chen, B. Liu, X. R. Deng, Y. Wei, J. Xia, B. G. Xing, P. A. Ma, J. Lin, *Adv. Sci.* **2017**, *4*, 1600540; c) X. Q. Yang, H. Hong, J. J. Grailer, I. J. Rowland, A. Javadi, S. A. Hurley, Y. L. Xiao, Y. A. Yang, Y. Zhang, R. Nickles, W. B. Cai, D. A. Steeber, S. Q. Gong, *Biomaterials* **2011**, *32*, 4151.

[24] a) A. Schudel, D. M. Francis, S. N. Thomas, *Nat. Rev. Mater.* **2019**, *4*, 415; b) J. Xiang, L. Xu, H. Gong, W. Zhu, C. Wang, J. Xu, L. Feng, L. Cheng, R. Peng, Z. Liu, *ACS Nano* **2015**, *9*, 6401.

[25] J. Xie, C. Yang, Q. Liu, J. Li, R. Liang, C. Shen, Y. Zhang, K. Wang, L. Liu, K. Shezad, M. Sullivan, Y. Xu, G. Shen, J. Tao, J. Zhu, Z. Zhang, *Small* **2017**, *13*, 1701741.

[26] M. Speir, A. Authier-Hall, C. R. Brooks, K. J. Farrand, B. J. Compton, R. J. Anderson, A. Heiser, T. L. Osmond, C. W. Tang, J. A. Berzofsky, M. Terabe, G. F. Painter, I. F. Hermans, R. Weinkove, *Sci. Rep.* **2017**, *7*, 14273.

[27] H. X. Ji, E. Y. Chang, K. Y. Lin, R. J. Kurman, D. M. Pardoll, T. C. Wu, *Int. J. Cancer* **1998**, *78*, 41.

[28] J. B. Liao, J. Publicover, J. K. Rose, D. DiMaio, *Clin. Vaccine Immunol.* **2008**, *15*, 817.

[29] H. Wang, A. J. Najibi, M. C. Sobral, B. R. Seo, J. Y. Lee, D. Wu, A. W. Li, C. S. Verbeke, D. J. Mooney, *Nat. Commun.* **2020**, *11*, 5696.